ORIGINAL ARTICLE

Quantitation of myocardial blood flow and myocardial flow reserve with ^{99m}Tc-sestamibi dynamic SPECT/CT to enhance detection of coronary artery disease

Bailing Hsu · Fu-Chung Chen · Tao-Cheng Wu · Wen-Sheng Huang · Po-Nien Hou · Chien-Cheng Chen · Guang-Uei Hung

Abstract

Purpose Conventional dual-head single photon emission computed tomography (SPECT)/CT systems capable of fast dynamic SPECT (DySPECT) imaging have a potential for flow quantitation. This study introduced a new method to quantify myocardial blood flow (MBF) and myocardial flow reserve (MFR) with DySPECT scan and evaluated the diagnostic performance of detecting coronary artery disease (CAD) compared with perfusion using invasive coronary angiography (CAG) as the reference standard.

Methods This study included 21 patients with suspected or known CAD who had received DySPECT, ECG-gated SPECT (GSPECT), and CAG (13 with ≥50 % stenosis in any vessel; non-CAD group: 8 with patent arteries or <50 % stenosis). DySPECT and GSPECT scans were performed on a widely used dual-head SPECT/CT scanner. The DySPECT imaging protocol utilized 12-min multiple back-and-forth gantry rotations during injections of ^{99m}Tc-sestamibi (MIBI) tracer at rest or dipyridamole-stress stages. DySPECT images were reconstructed with full physical corrections and converted to the physical unit of becquerels per milliliter. Stress MBF (SMBF), rest MBF (RMBF), and MFR were quantified by a one-tissue compartment flow model using time-activity curves derived from DySPECT images. Perfusion images were processed for GSPECT scan and interpreted to obtain summed stress score (SSS) and summed difference score (SDS). Receiver-operating characteristic (ROC) analyses were conducted to evaluate the diagnostic performance of flow and perfusion.

Results Using the criteria of ≥50 % stenosis as positive CAD, areas under the ROC curve (AUCs) of flow assessment were overall significantly greater than those of perfusion. For patient-based analysis, AUCs for MFR, SMBF, SSS, and SDS were 0.91±0.07, 0.86±0.09, 0.64±0.12, and 0.59±0.13. For vessel-based analysis, AUCs for MFR, SMBF, SSS, and SDS were 0.81±0.05, 0.76±0.06, 0.62±0.07, and 0.56±0.08, respectively.

Conclusion The preliminary data suggest that MBF quantitation with a conventional SPECT/CT system and the flow quantitation method is a clinically effective approach to enhance CAD detection.

Bailing Hsu and Fu-Chung Chen contributed equally to this work.

B. Hsu
Nuclear Science and Engineering Institute, University of Missouri-Columbia, Columbia, MO, USA

F.-C. Chen · C.-C. Chen (✉)
Section of Cardiology, Department of Internal Medicine, Show Chwan Memorial Hospital, Changhua, Taiwan
e-mail: q540925@gmail.com

T.-C. Wu
Section of Cardiology, Department of Internal Medicine, Taipei Veterans General Hospital, Taipei, Taiwan

W.-S. Huang
Department of Medical Research & Department of Nuclear Medicine, Changhua Christian Hospital, Changhua, Taiwan

P.-N. Hou · G.-U. Hung (✉)
Department of Nuclear Medicine, Chang Bing Show Chwan Memorial Hospital, 6 Lukon Road, Lukong Town, Changhua Shien 505, Taiwan
e-mail: 106143@gmail.com

G.-U. Hung
Department of Medical Imaging and Radiological Science, Central Taiwan University of Science and Technology, Taichung, Taiwan

G.-U. Hung
Department of Biomedical Imaging and Radiological Science, China Medical University, Taichung, Taiwan

Introduction

Besides the standard myocardial perfusion imaging (MPI) with single photon emission computed tomography (SPECT), noninvasive assessment of absolute myocardial blood flow (MBF) with positron emission tomography (PET) in milliliters per minute per gram and myocardial flow reserve (MFR) derived from stress to rest flow ratio has been continuously emerging as a clinical tool to detect the early stage of coronary atherosclerosis, stratify risks for cardiac events, and predict patient outcomes [1–7]. It has been reported that adding PET flow information to the relative perfusion imaging provides incremental diagnostic value for detection of coronary artery disease (CAD) [8–10] as PET flow itself can be an independent indicator of multivessel CAD [11, 12], representing a comprehensive tool to evaluate microvascular dysfunction with or without conventional cardiac risks [13, 14].

Although PET flow quantitation has been clinically marked as a powerful tool for diagnosis and prognosis of CAD at various clinical stages [15–17], in reality, it is not generally available in many areas around the world (e.g., Asian countries). The main challenge is posed by the fact that the production of PET tracers demands either high start-up costs to install an on-site cyclotron within the hospital (^{15}O-water and ^{13}N-ammonia) which may only be economically affordable by large medical centers or relatively high ongoing costs to purchase commercial generators on a monthly basis (^{82}Rb) which may not be economically realistic for clinical utilization. As a result, PET flow imaging has not been embraced by healthcare systems in these areas. Myocardial perfusion SPECT with ^{99m}Tc-labeled myocardial perfusion tracers (^{99m}Tc-sestamibi and ^{99m}Tc-tetrofosmin) remains the clinical standard for MPI worldwide [18]. Thus, flow quantitation with SPECT, when available, may be a practical solution to overcome challenges confronted by PET imaging and to warrant a widespread clinical utilization. In fact, modern SPECT and SPECT/CT instrumentation has been improved to attain high temporal resolution for dynamic data acquisition, although this unique capability in the past was not well investigated to design relevant protocols for clinical utilization. Furthermore, iterative reconstruction techniques with full physical corrections [19, 20] and the past experience of PET flow imaging collectively affirm development of a quantitative method for MBF quantitation with SPECT imaging.

This work presents a new method to achieve SPECT flow quantitation with a widely used SPECT/CT scanner by utilizing information derived from quantified dynamic SPECT (DySPECT) images and a compartment flow model for flow calculation comparable to the established PET methods [21–23]. An integrated SPECT imaging protocol was developed to acquire both flow and perfusion data with the same tracer injections. The diagnostic performance of SPECT flow and perfusion was assessed by comparing both parameters to luminal stenosis confirmed by invasive coronary angiography (CAG).

Materials and methods

DySPECT data acquisition

DySPECT data and CT images for attenuation correction (AC) were acquired on a commercially available dual-head SPECT/CT scanner (Symbia T, Siemens Medical Solutions, Malvern, PA, USA). The scanner was equipped with 0.95-cm thickness of NaI(Tl) crystal for gamma photon detection and functioned to perform fast back-and-forth or continuous gantry rotation with a maximum speed of 10 s per rotation. In a DySPECT scan, the L-shaped detectors were rotated from the patient's right anterior oblique (RAO) to left posterior oblique (LPO) positions to acquire a full set of projections with 64 views within a 180°degree arc and returned from LPO to RAO to acquire another set of projection data, and so forth. A DySPECT scan consisted of $10 \times 10 + 5 \times 20 + 4 \times 60 + 1 \times 280$ s for a duration of 12 min, and in total, 20 back-and-forth rotations were acquired to produce 1,280 projection views by using acquisition parameters of continuous mode, circular orbit, low-energy high-resolution (LEHR) collimator, 64×64 matrix, 1.78 zoom factor, 5.39 mm pixel size, and multiple energy windows (126–154 keV and 109–125 keV). CT images for AC were acquired with a low radiation dose CT scan (120 keV, 35 mA, 12 s).

DySPECT image reconstruction

DySPECT images were reconstructed with ordered subsets expectation maximization (OSEM, 3 iterations/16 subsets) [24] incorporated with full physical corrections for scatter, attenuation, isotope decay, collimator blur, and image noise [25–29]. Prior to image reconstruction, scatter correction (SC) was performed by subtracting estimated scatter count density (counts in pixel) to generate scatter-corrected projection data with the formula as follows [25]:

$$S_P = \frac{W_p}{2W_S} \cdot P_S \tag{1}$$

where S_P is the estimated scatter count density in photopeak energy window (126–154 keV), and P_S represents count density in the scatter window (109–125 keV). W_P and W_s are their energy window width. Each view of projection data was then normalized with the duration of their

corresponding rotation and an exponential factor depicting isotope decay as follows:

$$\frac{1}{D} \cdot exp^{[0.693 \times t_{R,A}/T_{Tc\text{-}99m}]} \quad (2)$$

where D is the duration of a rotation, and $t_{R,A}$ is the time stamp relative to the starting point of the DySPECT scan and indexed by the rotation and projection angle. T_{Tc99m} is the physical half-life of the ^{99m}Tc isotope. For AC, CT images were converted to 140-keV μ-map using the conversion formula as follows [26]:

$$\mu_{140} = \mu_{water} \cdot \left(\frac{HU}{1000} + 1.0\right) \text{ for } HU < 0$$
$$\mu_{140} = \mu_{water} \cdot \left(0.665 \cdot \frac{HU}{1000} + 1.0\right) \text{ for } HU \geq 0 \quad (3)$$

where HU is Hounsfield unit in CT images, and $\mu_{water} = 0.154$ cm^{-1} is the attenuation coefficient of water for 140 keV photons. To implement AC, an attenuation matrix functioned to record photon attenuation for image pixels pointing to all projection angles was pre-calculated and then applied to pre-updated images in the forward projection step of OSEM. Prior to AC, μ-map and DySPECT images were fused to verify transmission/emission misregistration by searching unregistered heart locations in both images (e.g., any part of myocardium locations in lung fields of the μ-map). Manual realignment was performed to shift the μ-map for misregistration correction before generating the attenuation matrix. For resolution recovery (RR) of images, depth-dependent point spread functions were physically measured for the SPECT/CT system and applied in the forward projection step of OSEM [27]. Noise suppression (NS) for images was achieved by implementing a statistical method to model Poisson noise in the reconstruction process [28, 29]. For the remaining DySPECT images, the residual activity in the myocardium from the stress injection was estimated from images of the first frame and propagated to subtract the residual myocardial uptake in the subsequent frames.

Assessment of image resolution

To verify the spatial resolution of reconstructed images, seven point sources with 21.1 MBq ^{99m}Tc activity on average for each source were lined up 5 cm apart to create angularly varied distances (17.2–53.9 cm) during the DySPECT acquisition. Prior to image reconstruction, dynamic projection views were summed to create a single set of static projection data. Images were then reconstructed with OSEM + RR. To measure the spatial resolution, images were resampled to a smaller pixel size of 1.35 mm. Line profiles of ^{99m}Tc activity were then obtained by drawing straight lines across the center

of point sources on orthogonal planes in resampled images. For each point source, line profiles were fitted with a Gaussian function to measure image resolution presented by the full-width at half-maximum (FWHM) in millimeters.

## Determination of conversion factor to becquerels per milliliter

The conversion factor serves to translate the unit of counts per second per pixel (cps/pixel) in reconstructed images to the physical unit of becquerels per milliliter. An assessment of camera linearity was performed with a cylindrical phantom (radius 16 cm, height 20 cm) initially filled in 1,731.6 MBq ^{99m}Tc water solution. During 24.7 h, 14 DySPECT scans were acquired within every 1–3 h with the count rate dropping from 150 to 10 kcps in both detectors. Each dynamic projection datum was processed with SC and normalization and then integrated to create static projection data by weighting the duration of the individual rotation to the total time of the DySPECT scan. Images were reconstructed with additional corrections of AC, RR, and NS as previously described. A cylindrical region of interest (ROI) was drawn across five image slices (slice thickness 5.39 mm) from the center of the phantom as 102.7 cm^3 and placed in phantom images to generate mean pixel values in the unit of counts per second per pixel. They were compared with known activity concentrations in the unit of becquerels per milliliter. A linear regression was performed to obtain the conversion factor as the slope of two variables.

SPECT flow quantitation

To quantify SPECT flow, we utilized the quantitative method built in a PET software package (FlowQuant, University of Ottawa Hospital, Ottawa, ON, Canada) [30]. The method employed a one-tissue compartment flow model to calculate kinetic parameters (K_1 and k_2) from the time-activity curve (TAC) obtained in regions of the left ventricle and atrium and myocardial tissue as follows:

$$C_{myo}(t) = FBV \cdot C_a(t) + (1-FBV) \cdot K_1 e^{-k_2 t} \otimes C_a(t) \quad (4)$$

where K_1 (ml/min per g) and k_2 (min^{-1}) characterize the rate of tracer uptake from blood to myocardial tissue and the rate of tracer washout from the tissue, respectively. $C_{myo}(t)$ is the measured activity concentration in the myocardium obtained from DySPECT images, assumed to consist of arterial blood input $C_a(t)$ and true myocardial uptake as a convoluted function of K_1, k_2, and $C_a(t)$. FBV refers to the fractional blood volume in $C_m(t)$ coming from $C_a(t)$, and $(1\text{-}FBV)$ is the
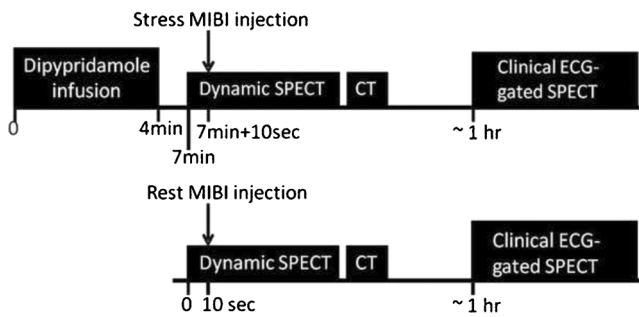
Fig. 1 A comprehensive imaging protocol integrating DySPECT with clinical GSPECT using the same rest and stress MIBI injections

rest of the fraction contributed from the true myocardial uptake. By applying the process of curve fitting, K_1, k_2, and FBV were solved to numerical values. MBF (ml/min per g) was then calculated from K_1 with additional

compensation for tracer extraction, E, in the myocardium as follows:

$$K_1 = MBF \cdot E(MBF) = MBF \cdot \left(1 - a \cdot e^{-\beta/MBF}\right) \quad (5)$$

where α and β are physiological parameters derived from the effective capillary permeability surface (PS) area product (ml/min per g) counting E as a function of MBF [31, 32]. This study utilized the ^{99m}Tc-sestamibi (MIBI) extraction fraction curve reported from an animal study ($\alpha=0.87$ and $\beta=0.44$) [23, 33]. To compensate for the physiological variance at rest stage, rest MBF was additionally corrected for the baseline heart rate and blood pressure by a factor of rate pressure product/10,000 bpm × mmHg [35]. MFR was calculated as the ratio of stress MBF (SMBF) to rest MBF (RMBF). Flow values of the entire myocardium were then presented in polar

Fig. 2 *Top*: Schematic illustration of SPECT scan with camera gantry rotated around 7 point sources from positions of RAO, LAO, anterior (ANT), lateral (LAT) to LPO and returned from LPO to RAO, and so forth. d_1 and d_7 are distances of point 1 and point 7 from detector surfaces. Distances of other sources are in between. *Middle*: The reconstructed images with OSEM or OSEM + RR for 7 points. *Bottom*: Corresponding image resolution presented in FWHM (mm)
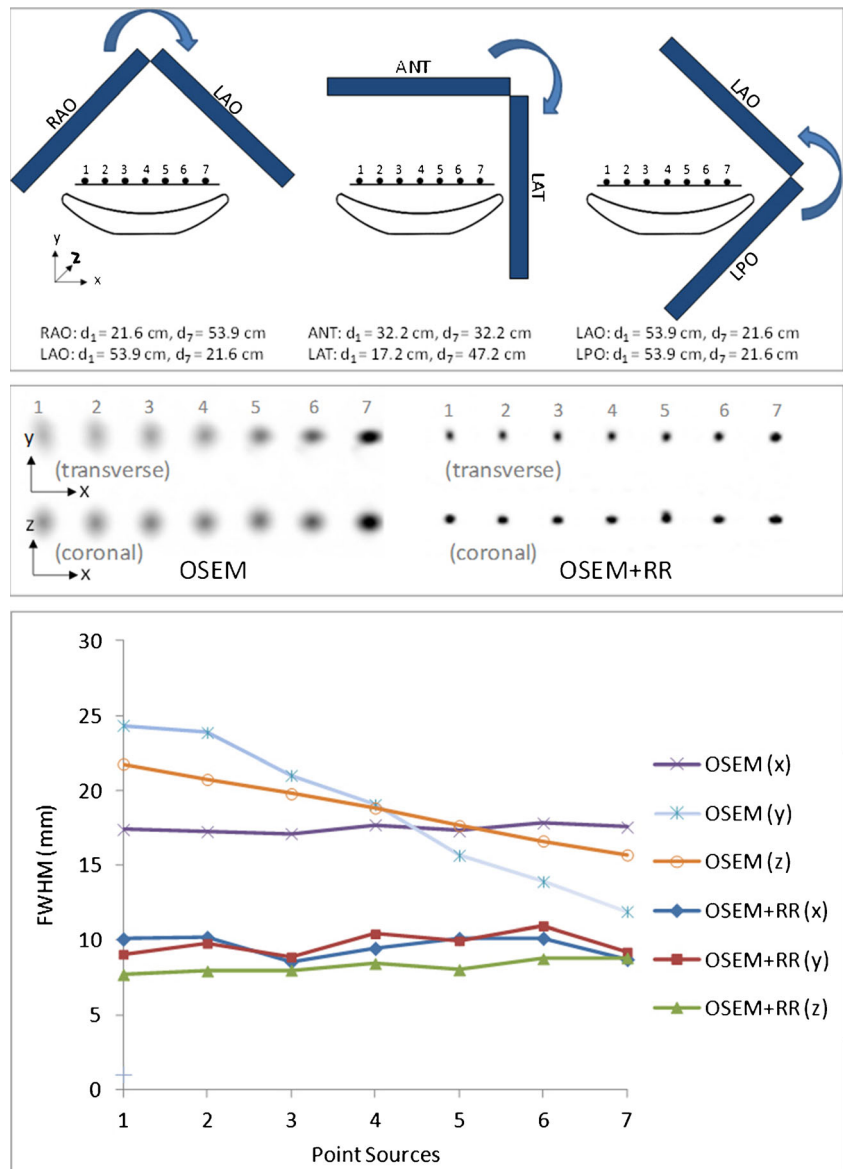
maps to calculate global MBF and MFR and for regional MBF and MFR in three coronary territories.

Patient population

This study included 21 patients with suspected or known CAD who had received DySPECT and ECG-gated SPECT (GSPECT) scans and CAG procedure (13 patients with ≥50 % stenosis in any vessel and 8 with patent arteries or <50 % stenosis). Each research subject agreed to sign a written consent approved by the Institutional Research Ethics Board in Show Chwan Memorial Hospital, Changhua, Taiwan.

Integrated SPECT imaging protocol

This study utilized the same MIBI injections for DySPECT and GSPECT scans. After proper patient preparation and giving the patient 500 ml water, a CT scout scan was performed to position the patient's heart inside the SPECT field of view. Dipyridamole vasodilator was infused for 4 min to achieve hyperemic myocardial flow with a dose of 0.56 mg/kg. After waiting for an additional 3 min, DySPECT was started and followed by a 370 MBq MIBI dose injection within 10 s. A low-dose CT for AC then followed for stress AC. After the completion of the stress DySPECT scan, the patient got off the scanner and returned for the routine clinical stress GSPECT within 45–60 min. After 3 h, at physiological rest state, the DySPECT scan was repeated with the same imaging setup and an injection of 1,000 MBq MIBI. A second low-dose CT scan then followed for rest AC. The routine clinical rest GSPECT was performed within 45–60 min thereafter. The integrated SPECT imaging protocol is illustrated in Fig. 1.

Analysis of perfusion images

Perfusion images were processed without and with AC (combined with SC, RR, and NS) using the standard platform provided by the vender (syngo, Siemens, USA). Non-AC and AC image sets were interpreted simultaneously by two experienced nuclear medicine physicians to score perfusion defects with a 5-point scale (0=normal, 1=mildly reduced, 2=moderately reduced, 3=severely reduced, and 4=absent uptake) for 17 segments [35]. Summed stress score (SSS) and summed rest score (SRS) were calculated by adding individual segmental scores and utilized to derive summed difference score (SDS) as SSS − SRS.

Invasive coronary angiography

CAG was performed according to the standard clinical procedure for all study subjects within 21±18 days (0–73). The percentage of luminal diameter stenosis in coronary arteries was quantitatively measured with a commercial software

(Innova 2100-IQ, GE Healthcare, Wauwatosa, WI, USA) operated by an experienced cardiologist. Positive CAD was defined as at least one lesion causing ≥50% luminal narrowing (obstructive lesion) in any vessel of left anterior descending (LAD), left circumflex (LCX), and right coronary artery (RCA) territories, otherwise non-CAD as patent or only <50 % luminal narrowing (nonobstructive lesion) in all of the three coronary arteries.

Statistical analysis

Continuous variables from image analysis were expressed as mean ± standard deviation, tested by Student's t test and analyzed with receiver-operating characteristic (ROC) statistics. Noncontinuous variables from patient clinical characteristics were expressed in number and percentage. Using CAG findings as the reference standard, patient-based (PB) and vessel-based (VB) ROC analyses were performed to retrospectively analyze the area under the curve (AUC) for SMBF, MFR, SSS, and SDS. The associated cutoff value to separate normal and abnormal groups for each index was then determined to generate largest AUC. Pairwise comparison for flow and perfusion
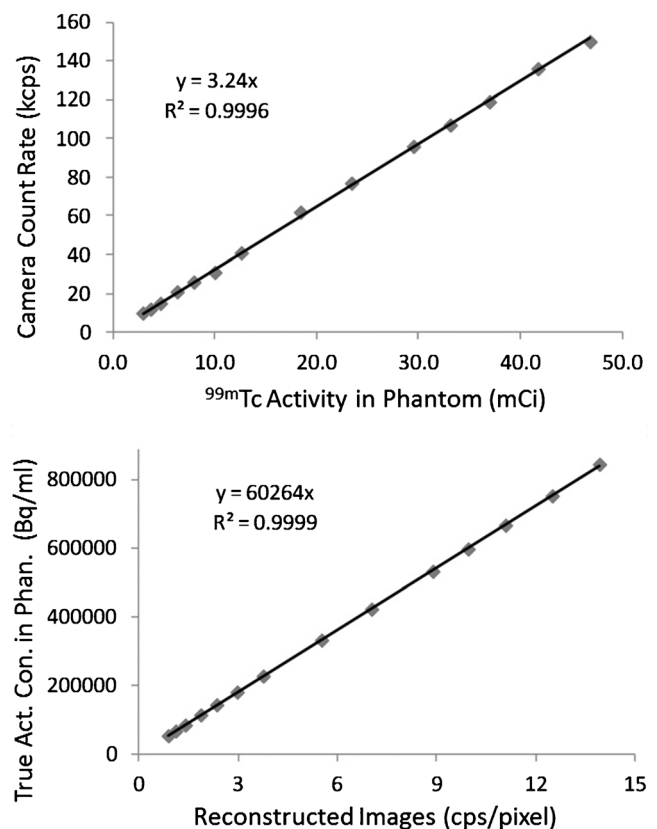
Fig. 3 *Top*: Linear regression of SPECT camera count rate and ^{99m}Tc activity in the phantom. *Bottom*: Linear regression of pixel value in reconstructed images in cps/pixel and true ^{99m}Tc concentration in Bq/ml in the phantom

Fig. 4 An example of 20 dynamic projection views acquired at RAO (**a**), ANT (**b**), ANT (**c**), and LPO (**d**) positions from a rest DySPECT scan. **e** Mean myocardial count density at the ANT position calculated for rest and stress DySPECT scans from all study subjects
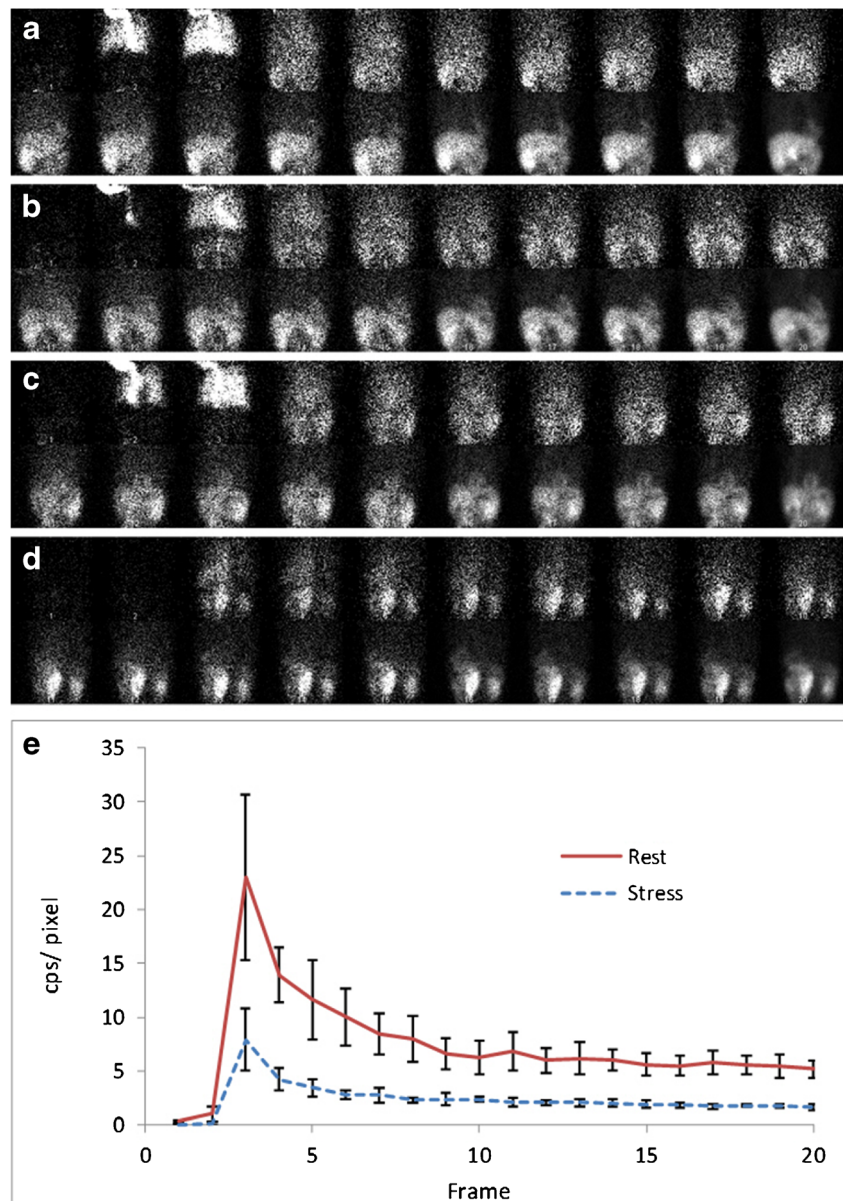
AUCs was conducted to evaluate the difference of diagnostic performance between quantitative flow and perfusion. A p value <0.05 was considered statistically significant.

Results

When images were reconstructed with OSEM only, the image resolution (FWHM) for seven point sources were 17.1–17.8 (mean = 17.4), 11.9–24.3 (18.5), and 15.7–21.8 mm (18.7) in x, y, and z directions as highly distance-dependent and non-isotropic. With OSEM + RR, the image resolution was improved to being less dependent on distance and more isotropic as 8.6–10.1 (9.6), 9.1–10.9 (9.7), and 7.7–8.8 mm (8.2) in

three directions, respectively (Fig. 2). Line profiles for point sources obtained from OSEM and OSEM + RR images overall had excellent correlation coefficients ($R^2 > 0.99$) as regressed with the Gaussian function.

The relation of count rate of detectors and ^{99m}Tc activities in the phantom was completely linear ($R^2 = 0.999$) as no count loss was verified up to 150 kcps count rate (Fig. 3). Mean pixel values in reconstructed images were perfectly linear to activity concentrations in the phantom ($R^2 = 0.999$) to give the conversion factor as 60,264 Bq/ml per cps/pixel.

With the injection of 370 MBq MIBI for stress and 1,000 MBq for rest, the average count density in the left ventricular region during the phase of MIBI activity filling into the left ventricular cavity was 8.4±3.2 cps/pixel for stress and 24.4±8.1 cps/pixel for rest. The peak count rate reported

Fig. 5 An example of rest and stress TACs obtained from the left ventricular cavity and the overall myocardium in DySPECT images. *Letters* present time frames and their corresponding images in the vertical long axis view
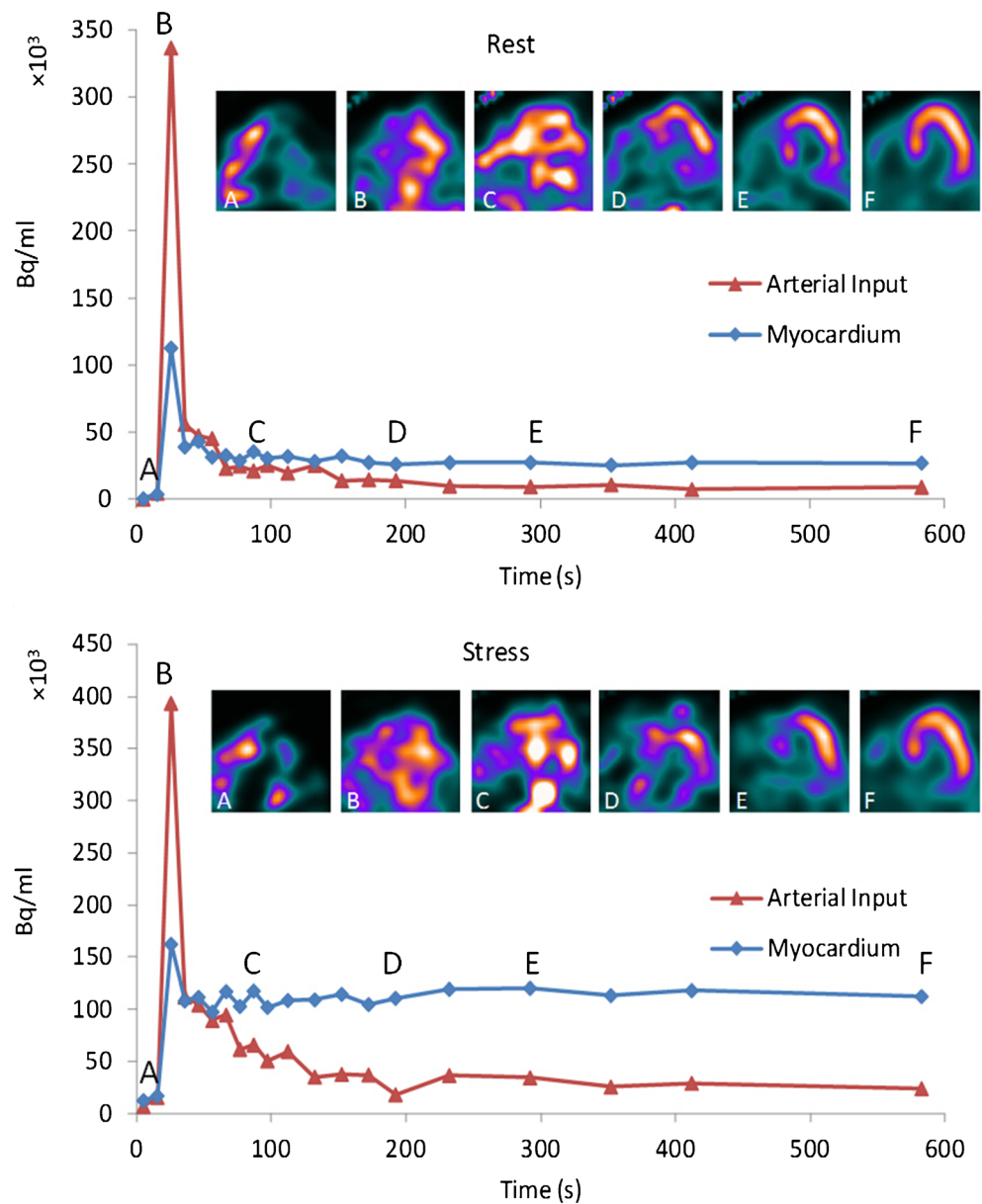
from the SPECT camera system was 36.2±9.8 kcps for stress and 103±28.6 kcps for rest. As myocardial uptake was stabilized in the last frame, average count density in the myocardial region was 1.75±0.17 cps/pixel for stress and 5.17±0.80 cps/pixel for rest as presented in Fig. 4. An example of rest and stress reconstructed DySPECT images in the vertical long axis view and corresponding TACs obtained from the left ventricular cavity and the overall myocardium can be found in Fig. 5.

Clinical characteristics of 21 study subjects are shown in Table 1 [34]. In the CAD group, 13 of them (62 %) presented ≥50 % luminal stenosis in any of the major coronary arteries as 5 one-vessel CAD, 4 two-vessel CAD, and 4 three-vessel CAD. There were a total of 38 obstructive lesions in 25 coronary artery territories as 21 lesions in LAD, 11 lesions in LCX, and 6 lesions in RCA. In the non-CAD group, only

one nonobstructive lesion (stenosis = 30 %) was found in LAD, and the rest of the arteries were patent. The list of luminal stenosis and associated locations in vessels is shown in Table 2.

Global kinetic, flow, and perfusion parameters for CAD and non-CAD groups are shown in Table 3. Global rest K_1 and RMBF in these two groups were similar, while global stress K_1, SMBF, and MFR in the CAD group were significantly lower than those of the non-CAD group (Fig. 6). SRS, SSS, and SDS for the CAD group were also lower, but the difference was not statistically significant. ROC curves of SMBF, MFR, SSS, and SDS for PB and VB analyses are displayed in Fig. 7. AUC and pairwise comparison between flow values and perfusion scores are shown in Table 4.

Table 1 Patient characteristics (*n*=21)

Characteristics	Data
Age	73±7
Men	12 (57 %)
Body mass index	25.7±5.6
Hypertension	14 (67 %)
Diabetes	5 (24 %)
Hyperlipidemia	10 (48 %)
Tobacco use	3 (14 %)
Family history of CAD	4 (19 %)
Prior percutaneous coronary intervention	6 (29 %)
Prior coronary artery bypass grafting	0
Prior myocardial infarction	4 (19 %)

In PB analysis, MFR AUC was significantly greater than those of SSS and SDS. SMBF AUC was greater, but not

Table 2 List of severity of luminal narrowing measured by CAG for CAD patients who had stenosis ≥50 % in any of the vessels with diameters ≥2.0 mm

Number	LAD	LCX	RCA
1	P: 30 % D: 70 %	NS	NS
2	OM1: 70 %	NS	NS
3	D: 70 %	NS	NS
4	P: 60 %	NS	NS
5	M: 70 % D2: 85 %	NS	NS
6	O: 75 % P: 70 % (IS)	O: 80 % M: 80 %	NS
7	P: 100 % M: 100 % D: 100 % D1: 80 %	OM1: 95 %	NS
8	P: 50 %	NS	P: 80 %
9	P: 80 %	OM2: 70 %	NS
10	M: 75 % D: 70 % (IS)	P: 100 % M: 100 % D: 100 %	P: 100 % M: 100 % D: 100 %
11	D: 80 %	D: 50 %	PL: 80 %
12	D1: 90 %	M: 90 % D: 100 % OM1: 50 %	PD: 80 %
13	P: 70 % M: 80 % D1: 80 % S1: 90 % S2: 80 %	P: 70 % OM1: 70 %	M: 80 % D: 85 %

O orifice, *P* proximal, *M* middle, *D* distal, *D1* diagonal 1, *D2* diagonal 2, *S1* septal 1, *S2* septal 2, *OM1* obtuse marginal 1, *OM2* obtuse marginal 2, *PD* posterior descending, *PL* posterior left, *NS* no stenosis

Table 3 Global kinetic parameters, flow values, and perfusion scores in CAD and non-CAD groups

	non-CAD	CAD	*p* value
Rest K_1 (ml/min per g)	0.40±0.06	0.44±0.11	0.271
Stress K_1 (ml/min per g)	0.62±0.76	0.47±0.16	0.022
Rest K_2 (min^{-1})	0.094±0.022	0.104±0.037	0.50
Stress K_2 (min^{-1})	0.145±0.017	0.114±0.055	0.149
SMBF (ml/min per g)	2.36±0.40	1.42±0.97	0.021
RMBF (ml/min per g)	0.81±0.27	0.93±0.48	0.283
MFR	3.37±0.82	1.61±0.88	<0.001
SSS	1.9±1.6	6.7±7.1	0.076
SRS	0.6±0.7	3.8±5.3	0.112
SDS	1.3±1.2	2.8±2.9	0.179

statistically significant. The cutoff criterion to define a patient with CAD was ≤2.0 MFR with sensitivity (SEN) = 84.6 %, specificity (SPE) = 100 %, positive predictive value (PPV) = 100 %, and negative predictive value (NPV) = 80.0 % (power = 0.9). The cutoff criterion for SMBF was ≤1.96 ml/min per g with SEN = 84.5 %, SPE = 100 %, PPV = 100 %, and NPV = 79.6 % (power = 0.8). There was no statistical difference between the MFR AUC and SMBF AUC or SSS AUC and SDS AUC. The cutoff criterion for SDS was ≥2 with SEN = 69.2 %, SPE = 70.1 %, PPV = 78.9 %, and NPV = 58.3 % (power<0.8). The cutoff criterion for SSS was ≥3 with SEN = 69.2 %, SPE = 62.5 %, PPV = 74.9 %, and NPV = 55.5 % (power<0.8). Figure 8 shows an example of three-vessel CAD confirmed by CAG and uncovered as globally severe ischemic myocardium by stress MBF = 0.54 and MFR = 1.0, but defined as within normal limits by perfusion images.

In VB analysis, MFR AUC was significantly greater than those of SSS and SDS. SMBF AUC was also greater but not significant. The difference of MFR AUC vs SMBF AUC or SSS AUC or SDS AUC was overall not significant. The cutoff criterion for MFR to determine a vessel with CAD was ≤1.70 with SEN = 76.0 %, SPE = 84.2, PPV = 76.0, and NPV = 84.2 % (power=0.95). The cutoff criterion for SBMF was ≤1.51 ml/min per g with SEN = 80.0 %, SPE = 76.3 %, PPV = 69.0 %, and NPV = 85.2 % (power=0.95). The cutoff criterion for SDS was ≥1 with SEN = 60.0 %, SPE = 52.6 %, PPV = 45.5 %, and NPV = 66.6 % (power<0.8). The cutoff criterion for SSS was ≥2 with SEN = 56.0 %, SPE = 62.8 %, PPV = 49.7 %, and NPV = 68.4 % (power<0.8).

Discussion

In this study, we presented a new method to quantify MBF and MFR with MIBI myocardial perfusion tracer, a conventional SPECT/CT system capable of DySPECT scan, iterative reconstruction with full physical corrections for quantitative

Fig. 6 Individual plot of global/vessel SMBF and MFR in non-CAD and CAD groups
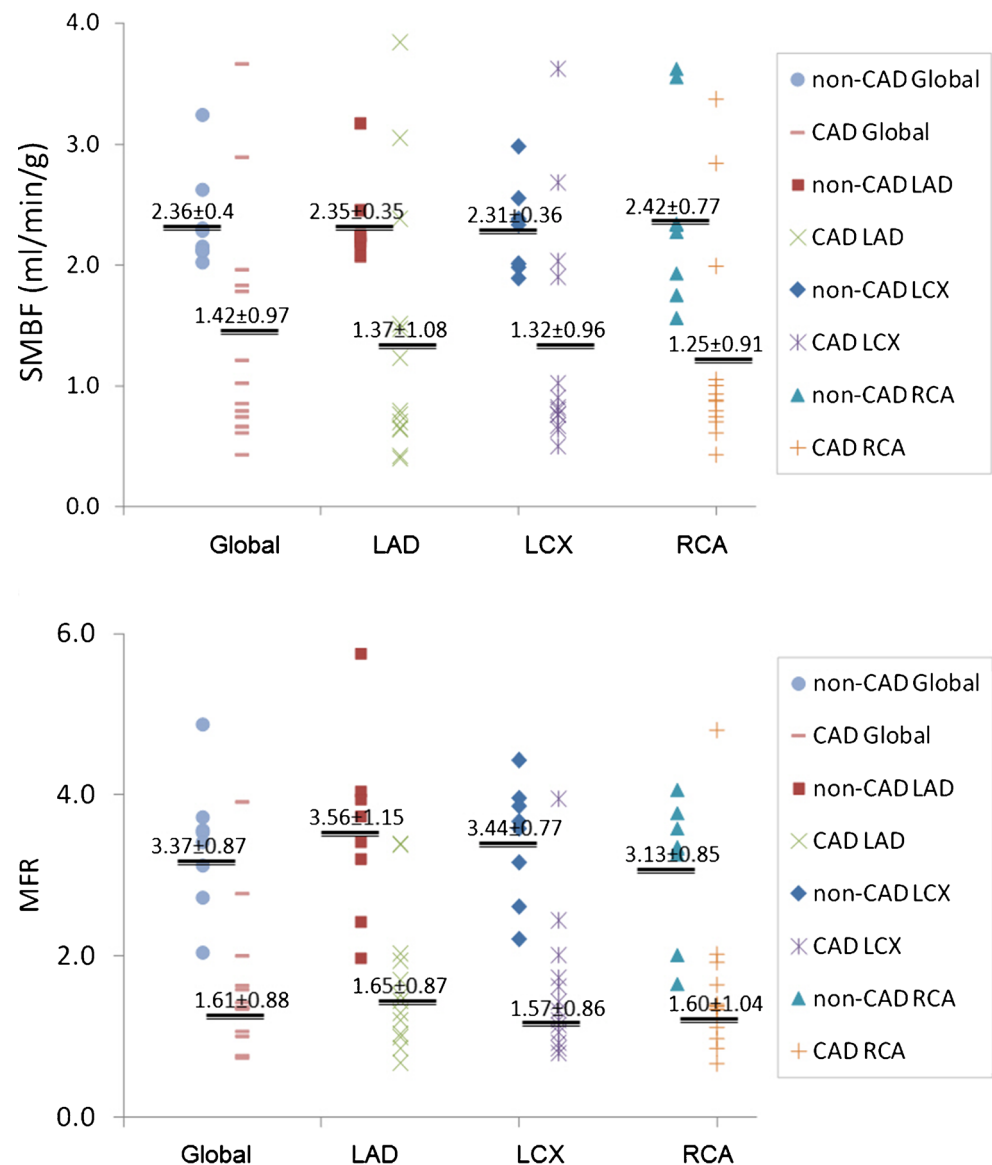
images in becquerels per milliliter, and kinetic modeling for flow calculation. Unlike those previous SPECT studies [36–40], our method to derive MFR from absolute MBF (in ml/min per g) was highly comparable with PET methods [21–23, 30]; thus, the performance of flow calculation may be more consistent in terms of avoiding physical interferences. In this study, the spatial resolution of DySPECT images was improved to twofold (from 18.2 to 9.2 mm on average) with OSEM+RR which provided an optimal image resolution to extract arterial and myocardial TACs. However, this improved but imperfect resolution still caused a significant amount of spillover from the left ventricle to the myocardium when MIBI activity was filling the left ventricular cavity (Fig. 5). The spillover effect was parameterized as FBV in the flow model (Eq. 4). The value was reported in a range of 0.2–0.6, depending on the physical size of the myocardium. This study did not include an additional kinetic parameter, k_3, to depict

the interactive activity of the MIBI tracer and mitochondria using a two-tissue compartment model. In fact, the flow calculation often failed as k_3 was introduced, possibly due to the uncertainty from image noise, but further investigation would be needed for clarification. In contrast to PET imaging, which is proficient in simultaneously acquiring all projection (or sinogram) views while the tracer is still rapidly circulating in the patient, the nature of DySPECT imaging as fast as 10 s per rotation may not be proficient in tracing fast tracer movement in all projections as illustrated by the second frame of the LPO view in Fig. 4. However, this inconsistency was previously verified by a separate Monte Carlo simulation study and confirmed <10 % error in flow calculation with such temporal resolution [41]. In our study, MIBI doses for DySPECT imaging utilized clinical doses for GSPECT (stress: 370 MBq, rest: 1,000 MBq). The doses were sufficient to generate good image accuracy to extract TACs for patients
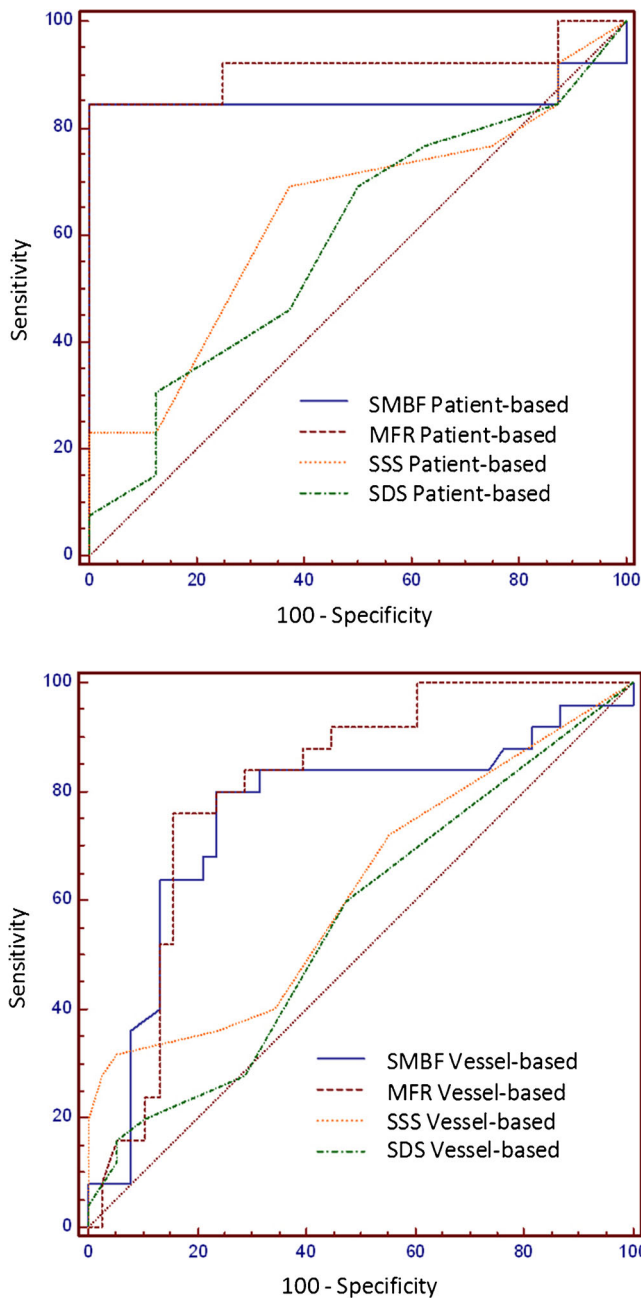
Fig. 7 PB and VB ROC curves of SMBF, MFR, SSS, and SDS to detect CAD using CAG as the reference standard

with 20.3–36.2 body mass index (BMI, average 25.7). For patients with a BMI greater than this range, BMI-adjusted MIBI dose may be considered if image accuracy is substantially degraded. Furthermore, because of using the same dose injections for DySPECT and GSPECT scans, the imaging protocol did not request giving extra radiation to patients, but only adding extra imaging time for the DySPECT scan while the patient was waiting; thus, the integrated imaging SPECT protocol can be efficient for clinical utilization. In DySPECT scans, elevated uptake in liver usually became detectable about 90–120 s after MIBI injection as shown in

Table 4 Difference of ROC AUC between flow and perfusion for 21 patients with CAG

	SMBF	MFR	SSS	SDS
PB AUC	0.86 ± 0.09 (95 % CI 0.64–0.97)	0.91 ± 0.07 (95 % CI 0.70–0.99)	0.64 ± 0.12 (95 % CI 0.40–0.83)	0.59 ± 0.13 (95 % CI 0.36–0.80)
	SMBF vs MFR p=0.548; SMBF vs SSS p=0.136; MFR vs SSS p=0.016; MFR vs SDS p=0.009; SSS vs SDS p=0.604	SMBF vs SDS p=0.077		
VB AUC	0.76 ± 0.06 (95 % CI 0.63–0.86)	0.81 ± 0.05 (95 % CI 0.69–0.80)	0.62 ± 0.07 (95 % CI 0.49–0.74)	0.56 ± 0.08 (95 % CI 0.43–0.69)
	SMBF vs MFR p=0.385; SMBF vs SSS p=0.140; MFR vs SSS p=0.033; MFR vs SDS p=0.246; SSS vs SDS p=0.246	SMBF vs SDS p=0.032; MFR vs SDS p=0.006		

CI confidence interval

Fig. 4. However, the impact of liver spillover to TAC accuracy should depend on its relative location to the myocardium and was varied patient by patient in our study. Under extreme conditions, the liver and myocardial inferior wall might share the same image voxel, and their boundary may become not differentiable. A protocol of routinely giving patients a substantial amount of water may be implemented to enlarge the stomach size in order to propel the liver away from the myocardium to eliminate the liver interference. As shown in Fig. 5, typical rest and stress TACs reached optimal clearance of MIBI activity in the left ventricular cavity and stabilized myocardial uptake at 5 min after MIBI injections; thus, it may be feasible to shorten the DySPECT scan time to 5 min to still provide sufficient data, but the impact on flow calculation needs further investigation.

In this study, the diagnostic performance of flow and perfusion in ROC analyses utilizing CAG as the reference standard favored flow to detect CAD. This finding is concordant with several previous PET studies using ^{13}N-ammonia or ^{82}Rb as flow tracers [8–10]. Figure 8 demonstrated a case with completely homogeneous perfusion images and no evidence of transient ischemic dilatation, but SMBF and MFR were overall below the CAD threshold, and CAG confirmed three-vessel CAD. Several studies also highlighted that myocardial perfusion SPECT was very limited to detect multivessel CAD (two or three) [42, 43]; thus, low diagnostic sensitivity (0.48) and underestimated CAD severity were observed. In our study, there was a relatively high prevalence of patients (8 of the 13 CAD patients; 62 %) with multivessel CAD confirmed by CAG. More likely the extent and severity of the perfusion

Fig. 8 A 71-year-old male patient with hyperlipidemia and no history of CAD complained of chest pain unrelated to increased physical activity. He was ordered to receive GSPECT with DySPECT scans for CAD evaluation. *Top*: The GSPECT scan revealed no evidence of myocardial perfusion abnormality on the stress/rest images, and no transient ischemic dilatation was found. *Middle*: The quantitative flow values from his DySPECT scan were SMBF = 0.54 ml/min per g, RMBF = 0.53 ml/min per g, and MFR = 1.0, which were extensively lower than the CAD thresholds (SMBF = 1.96 and MFR = 2.0) determined in this study. *Bottom*: Because of the concern of continuous symptoms, CAG was performed 31 days after the SPECT imaging. CAG confirmed severe luminal stenosis in LAD, LCX, and RCA coronary arteries as severe three-vessel CAD
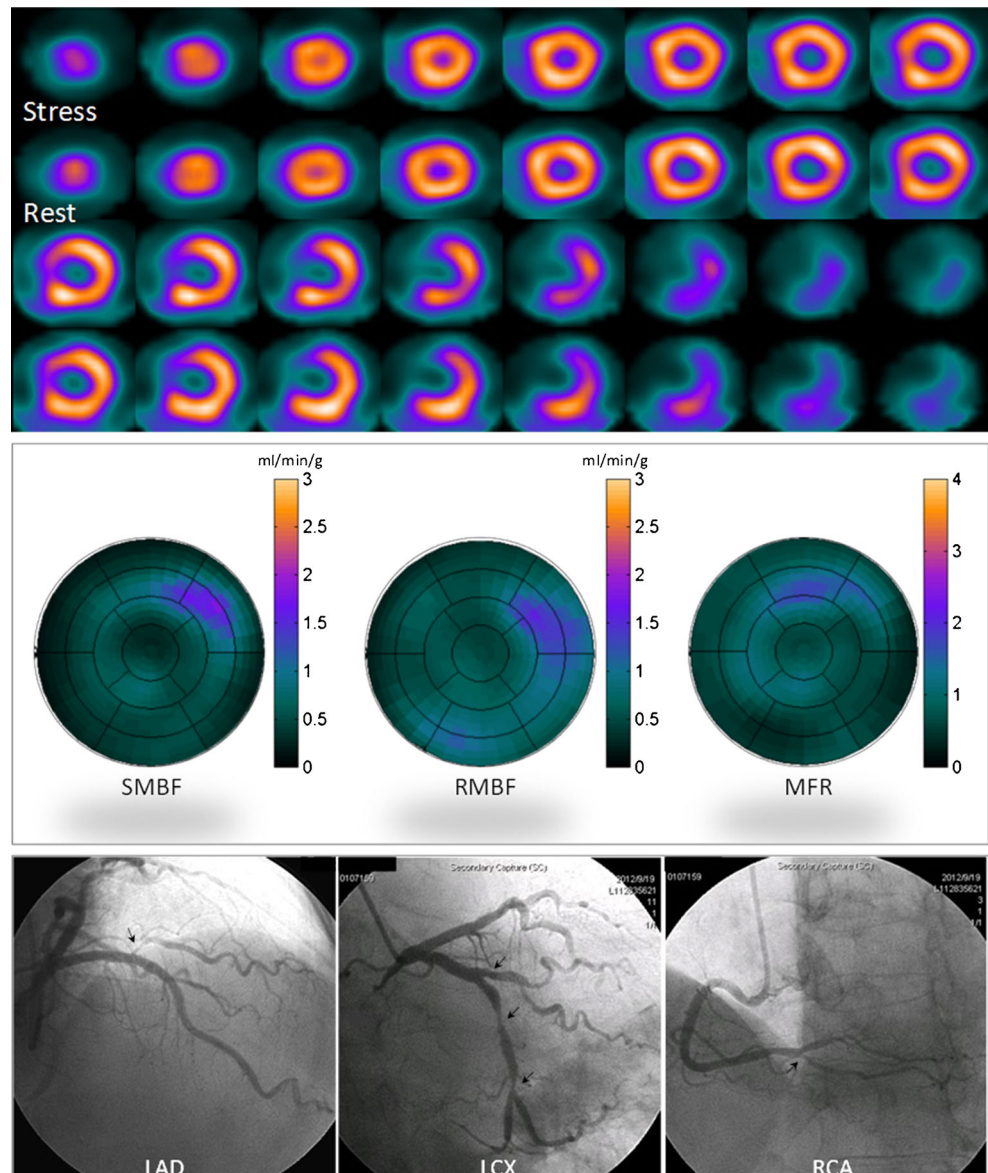
abnormality with perfusion scores in this population would also be underrated to report lower AUC values than those values (0.74–0.84) published in the literature [44, 45]. Due to the limited ability of perfusion images to differentiate between severe multivessel disease and normal perfusion, differences of SSS and SDS in the CAD and non-CAD groups were not statistically significant in our study. However, statistical differences of these two groups were achievable by the analysis of flow parameters (SMBF: $p=0.021$; MBF: $p<0.001$). Consequently, adding SPECT flow quantitation to the routine perfusion assessment may be substantially valuable to rule out an underestimated perfusion abnormality and potential false-negative diagnosis of multivessel CAD. In the future, clinical implementation of SPECT flow quantitation may be very important, particularly for Asian countries where myocardial PET tracers are unavailable or economically unaffordable and myocardial perfusion SPECT is still used as the main clinical tool for CAD diagnosis. The new method developed in this study for SPECT flow quantitation therefore may offer a simple and effective solution to fill in the gap.

Study limitation

This study adopted MIBI extraction from a nonhuman study to calculate MBF from K_1 for patients due to the reason that human extraction has not been available. Although not ideal, flow parameters with animal MIBI extraction were still able to differentiate between CAD and non-CAD patients. To address this imperfectness, our group is currently pursuing a comparative study of MIBI K_1 to ^{13}N-ammonia PET flow in the same healthy volunteers to obtain human MIBI extraction fraction data. Besides, this study did not address the impact of intra-scan patient motion to affect the accuracy of flow calculation, and motion correction algorithms were not implemented. A future study should be pursued to address this important issue. This study only included a limited number of patients ($n=21$) who had received MIBI DySPECT, GSPECT, and CAG for comparison. In fact, the statistical power of ROC analyses for this small group of patients still met the minimal criteria for statistical satisfaction (power $\geq$ 0.80). An extended study with large cohorts should be pursued to reconfirm the incremental value of SPECT flow quantitation found in this study.

Conclusion

Flow quantitation with quantitative dynamic SPECT is a superior method over myocardial perfusion SPECT for CAD detection as perfusion images often underestimate the extent and severity of perfusion abnormalities in the population with multivessel CAD. SPECT flow quantitation with the conventional SPECT/CT system is effective to enhance CAD detection without adding extra radiation burden to patients.

References

1. Murthy VL, Naya M, Foster CR, Hainer J, Gaber M, Di Carli G, et al. Improved cardiac risk assessment with noninvasive measures of coronary flow reserve. Circulation 2011;124:2215–24.
2. Ziadi MC, Dekemp RA, Williams KA, Guo A, Chow BJ, Renaud JM, et al. Impaired myocardial flow reserve on rubidium-82 positron emission tomography imaging predicts adverse outcomes in patients assessed for myocardial ischemia. J Am Coll Cardiol 2011;58:740–8.
3. Herzog BA, Husmann L, Valenta I, Gaemperli O, Siegrist PT, Tay FM, et al. Long-term prognostic value of 13N-ammonia myocardial perfusion positron emission tomography added value of coronary flow reserve. J Am Coll Cardiol 2009;54:150–6.
4. Czernin J, Barnard RJ, Sun KT, Krivokapich J, Nitzsche E, Dorsey D, et al. Effect of short-term cardiovascular conditioning and low-fat diet on myocardial blood flow and flow reserve. Circulation 1995;92: 197–204.
5. Dayanikli F, Grambow D, Muzik O, Mosca L, Rubenfire M, Schwaiger M. Early detection of abnormal coronary flow reserve in asymptomatic men at high risk for coronary artery disease using positron emission tomography. Circulation 1994;90:808–17.
6. Camici PG, Crea F. Coronary microvascular dysfunction. N Engl J Med 2007;356:830–40.
7. Reddy KG, Nair RN, Sheehan HM, Hodgson JM. Evidence that selective endothelial dysfunction may occur in the absence of angiographic or ultrasound atherosclerosis in patients with risk factors for atherosclerosis. J Am Coll Cardiol 1994;23:833–43.
8. Muzik O, Duvernoy C, Beanlands RS, Sawada S, Dayanikli F, Wolfe Jr ER, et al. Assessment of diagnostic performance of quantitative flow measurements in normal subjects and patients with angiographically documented coronary artery disease by means of nitrogen-13 ammonia and positron emission tomography. J Am Coll Cardiol 1998;31:534–40.
9. Hajjiri MM, Leavitt MB, Zheng H, Spooner AE, Fischman AJ, Gewirtz H. Comparison of positron emission tomography measurement of adenosine-stimulated absolute myocardial blood flow versus relative myocardial tracer content for physiological assessment of coronary artery stenosis severity and location. JACC Cardiovasc Imaging 2009;2:751–8.
10. Fiechter M, Ghadri JR, Gebhard C, Fuchs TA, Pazhenkottil AP, Nkoulou RN, et al. Diagnostic value of 13N-ammonia myocardial perfusion PET: added value of myocardial flow reserve. J Nucl Med 2012;53:1230–4.
11. Parkash R, deKemp RA, Ruddy TD, Kitsikis A, Hart R, Beauchesne L, et al. Potential utility of rubidium 82 PET quantification in patients with 3-vessel coronary artery disease. J Nucl Cardiol 2004;11:440–9.
12. Ziadi MC, Dekemp RA, Williams K, Guo A, Renaud JM, Chow BJ, et al. Does quantification of myocardial flow reserve using rubidium-

82 positron emission tomography facilitate detection of multivessel coronary artery disease? J Nucl Cardiol 2012;19:670–80.

13. Graf S, Khorsand A, Gwechenberger M, Novotny C, Kletter K, Sochor H, et al. Typical chest pain and normal coronary angiogram: cardiac risk factor analysis versus PET for detection of microvascular disease. J Nucl Med 2007;48:175–81.

14. Recio-Mayoral A, Rimoldi OE, Camici PG, Kaski JC. Inflammation and microvascular dysfunction in cardiac syndrome X patients without conventional risk factors for coronary artery disease. JACC Cardiovasc Imaging 2013;6:660–7.

15. Schelbert HR. Quantification of myocardial blood flow: what is the clinical role? Cardiol Clin 2009;27:277–89.

16. Schindler TH, Schelbert HR, Quercioli A, Dilsizian V. Cardiac PET imaging for the detection and monitoring of coronary artery disease and microvascular health. JACC Cardiovasc Imaging 2010;3:623–40.

17. Schelbert HR. Positron emission tomography measurements of myocardial blood flow: assessing coronary circulatory function and clinical implications. Heart 2012;98:592–600.

18. Vitola JV, Shaw LJ, Allam AH, Orellana P, Peix A, Ellmann A, et al. Assessing the need for nuclear cardiology and other advanced cardiac imaging modalities in the developing world. J Nucl Cardiol 2009;16:956–61.

19. Zeintl J, Vija AH, Yahil A, Hornegger J, Kuwert T. Quantitative accuracy of clinical 99mTc SPECT/CT using ordered-subset expectation maximization with 3-dimensional resolution recovery, attenuation, and scatter correction. J Nucl Med 2010;51:921–8.

20. Bailey DL, Willowson KP. An evidence-based review of quantitative SPECT imaging and potential clinical applications. J Nucl Med 2013;54:83–9.

21. Coxson PG, Huesman RH, Borland L. Consequences of using a simplified kinetic model for dynamic PET data. J Nucl Med 1997;38:660–7.

22. Lortie M, Beanlands RS, Yoshinaga K, Klein R, Dasilva JN, DeKemp RA. Quantification of myocardial blood flow with 82Rb dynamic PET imaging. Eur J Nucl Med Mol Imaging 2007;34:1765–74.

23. Klein R, Beanlands RS, deKemp RA. Quantification of myocardial blood flow and flow reserve: technical aspects. J Nucl Cardiol 2010;17:555–70.

24. Hudson HM, Larkin RS. Accelerated image reconstruction using ordered subsets of projection data. IEEE Trans Med Imaging 1994;13:601–9.

25. Ichihara T, Ogawa K, Motomura N, Kubo A, Hashimoto S. Compton scatter compensation using the triple-energy window method for single- and dual-isotope SPECT. J Nucl Med 1993;34:2216–21.

26. Bai C, Shao L, Da Silva AJ, Zhao Z. A generalized model for the conversion from CT numbers to linear attenuation coefficients. IEEE Trans Nucl Sci 2003;50:1510–5.

27. Liu S, Farncombe T. Collimator-detector response compensation in quantitative SPECT reconstruction. IEEE Nucl Sci Symp Conf Rec 2007;5:3955–60.

28. Soares EJ, Glick SJ, Hoppin JW. Noise characterization of block-iterative reconstruction algorithms: II. Monte Carlo simulations. IEEE Trans Med Imaging 2005;24:112–21.

29. Dutta J, Ahn S, Li Q. Quantitative statistical methods for image quality assessment. Theranostics 2013;3:741–56.

30. Klein R, Renaud JM, Ziadi MC, Thorn SL, Adler A, Beanlands RS, et al. Intra- and inter-operator repeatability of myocardial blood flow and myocardial flow reserve measurements using rubidium-82 PET and highly automated analysis program. J Nucl Cardiol 2010;17:600–16.

31. Renkin EM. Transport of potassium-42 from blood to tissue isolated mammalian skeletal muscles. Am J Physiol 1959;197:1205–10.

32. Crone C. The permeability of capillaries in various organs as determined by use of the 'indicator diffusion' method. Acta Physiol Scand 1963;58:292–305.

33. Leppo JA, Meerdink DJ. Comparison of the myocardial uptake of a technetium-labeled isonitrile analogue and thallium. Circ Res 1989;65:632–9.

34. Czernin J, Müller P, Chan S, Brunken RC, Porenta G, Krivokapich J, et al. Influence of age and hemodynamics on myocardial blood flow and flow reserve. Circulation 1993;88:62–9.

35. Tilkemeier PL, Cooke CD, Grossman GB, McCallister BD, Ward RP (2009) ASNC imaging guidelines for nuclear cardiology procedures: standardized reporting of radionuclide myocardial perfusion and function. Available via http://www.asnc.org.

36. Di Bella EV, Ross SG, Kadrmas DJ, Khare HS, Christian PE, McJames S, et al. Compartmental modeling of technetium-99m-labeled teboroxime with dynamic single-photon emission computed tomography: comparison with static thallium-201 in a canine model. Invest Radiol 2001;36:178–85.

37. Iida H, Eberl S, Kim KM, Tamura Y, Ono Y, Nakazawa M, et al. Absolute quantitation of myocardial blood flow with (201)Tl and dynamic SPECT in canine: optimisation and validation of kinetic modelling. Eur J Nucl Med Mol Imaging 2008;35:896–905.

38. Sugihara H, Yonekura Y, Kataoka K, Fukai D, Kitamura N, Taniguchi Y. Estimation of coronary flow reserve with the use of dynamic planar and SPECT images of Tc-99m tetrofosmin. J Nucl Cardiol 2001;8:575–9.

39. Christian TF, Peters K, Keck B, Allen J, Owens T, Borah B. Gated SPECT imaging to detect changes in myocardial blood flow during progressive coronary occlusion. Int J Cardiovasc Imaging 2008;24:269–76.

40. Ben-Haim S, Murthy VL, Breault C, Allie R, Sitek A, Roth N, et al. Quantification of myocardial perfusion reserve using dynamic SPECT imaging in humans: a feasibility study. J Nucl Med 2013;54:873–9.

41. Hung GU, Ljungberg M, Klein R, deKemp R, Hsu BL. The accuracy of fast dynamic cardiac SPECT acquisition: a Monte Carlo evaluation (abstract). J Nucl Med 2013;54:96P.

42. Bateman TM, Heller GV, McGhie AI, Friedman JD, Case JA, Bryngelson JR, et al. Diagnostic accuracy of rest/stress ECG-gated Rb-82 myocardial perfusion PET: comparison with ECG-gated Tc-99m sestamibi SPECT. J Nucl Cardiol 2006;13:24–33.

43. Berman DS, Kang X, Slomka PJ, Gerlach J, de Yang L, Hayes SW, et al. Underestimation of extent of ischemia by gated SPECT myocardial perfusion imaging in patients with left main coronary artery disease. J Nucl Cardiol 2007;14:521–8.

44. Guner LA, Karabacak NI, Cakir T, Akdemir OU, Kocaman SA, Cengel A, et al. Comparison of diagnostic performances of three different software packages in detecting coronary artery disease. Eur J Nucl Med Mol Imaging 2010;37(11):2070–8.

45. Arsanjani R, Xu Y, Hayes SW, Fish M, Lemley Jr M, Gerlach J, et al. Comparison of fully automated computer analysis and visual scoring for detection of coronary artery disease from myocardial perfusion SPECT in a large population. J Nucl Med 2013;54(2):221–8.